B. F. Feeny[1]
Department of Mechanical Engineering,
Michigan State University,
East Lansing, MI 48824
e-mail: feeny@egr.msu.edu

P. W. Sternberg
e-mail: pws@caltech.edu

C. J. Cronin
e-mail: cjc@caltech.edu

Division of Biology,
California Institute of Technology,
Pasadena, CA 91125

C. A. Coppola
Department of Mechanical Engineering,
Michigan State University,
East Lansing, MI 48824

Complex Orthogonal Decomposition Applied to Nematode Posturing

The complex orthogonal decomposition (COD), a process of extracting complex modes from complex ensemble data, is summarized, as is the use of complex modal coordinates. A brief assessment is made on how small levels of noise affect the decomposition. The decomposition is applied to the posturing of Caenorhabditis elegans, an intensively studied nematode. The decomposition indicates that the worm has a multimodal posturing behavior, involving a dominant forward locomotion mode, a secondary, steering mode, and likely a mode for reverse motion. The locomotion mode is closer to a pure traveling waveform than the steering mode. The characteristic wavelength of the primary mode is estimated in the complex plane. The frequency is obtained from the complex modal coordinate's complex whirl rate of the complex modal coordinate, and from its fast Fourier transform. Short-time decompositions indicate the variation of the wavelength and frequency through the time record. [DOI: 10.1115/1.4023548]

1 Introduction

In this work, we demonstrate the application of a method of decomposing complex modes, the complex orthogonal decomposition (COD) [1], to oscillatory bio-locomotion. In particular, the method is applied to sensed ensembles of the wavelike posturing movements of a nematode worm as it crawls. Nematodes are roundworms, nonsegmented worms with digestive, circulatory, and neuromuscular systems. Our focus is on *Caenorhabditis elegans*, a tiny (about 1 mm in length) nematode which lives freely in the soil. These worms crawl by generating a neuromuscular-mechanical wave, which, given their small size and low-frequency oscillation (typically a fraction of a Hz), has negligible inertial effects.

In 1998, *C. elegans* became the first animal whose entire genome was sequenced (The *C. elegans* Genome Sequencing Consortium, 1998). The genome consists of about 100 million DNA base pairs, and includes about 20 000 genes. As such, *C. elegans* is a very important model for animal biology and genetics in general. Studies of nematodes can have important implications for all animals, including humans. Since it has a short generation time (3 days) and a short life span (2–3 weeks), *C. elegans* is a valuable subject for studying development, neurobiology, and aging [2] (also http://www.wormbook.org).

Nematode locomotion has been useful as an assay for identifying genes and pathways underlying synaptic transmission and its regulation [3–7], and more recently to understand how locomotion is regulated; for example, by mechanosensors [8] and epidermal growth factor [9]. There has been much recent effort to understand and model the structural neuromuscular mechanics [10–14], and to understand the gaits [15–17]. Also, and perhaps most importantly, analysis of locomotion data is crucial for modeling the biomechanics and neural circuits controlling this process [10,11]. Automated systems now allow the posture of these worms to be extracted from video images [18], enabling further analysis of the movement [19]. COD provides an opportunity for further development of the nematode motion analysis toolbox. As such, in this work we apply the tool to decompose the wavelike movements of worms. The benefits of this analysis are to reveal different modes for different behavioral actions, and to isolate the locomotion mode, and separate its temporal and spatial variables, in calculating its wave parameters.

2 Complex Mode Decomposition

2.1 Background on the Decomposition Strategy. The method employed, COD, is a generalization of the well-known proper orthogonal decomposition (POD). POD, similar to singular value decomposition (SVD), is a tool for extracting modes that optimize the signal energy distribution in a set of measured time series. It has been used to characterize spatial coherence in turbulence and structures [20–22], the dimension of the dynamics [21–23], empirical modes for reduced order models [24,25], and in system identification [26,27]. POD, SVD, and similar tools have been compared for structural applications [28]. In specific circumstances, the POD produces the normal modes of a structure [29–32].

POD is particularly useful if extracting standing wave components, but is less suited for decomposing nonstanding wave components. The COD fills this void, as complex modes can be used to describe nonstanding and traveling waves [33]. Complex modal motions also occur in mechanical vibration systems with gyroscopic terms, general damping [34,35], and asymmetric stiffness matrices (flutter and friction).

2.2 Complex Modes and Wave Motions. The harmonic motion in a complex mode $\mathbf{z}(t) = e^{\alpha t}\mathbf{u}$, where $\mathbf{z}$ is a vector of particle positions, t is time, $\alpha = \gamma + \omega i$, and $\mathbf{u} = \mathbf{c} + \mathbf{d}i$ is a complex mode, with $\gamma, \omega, \mathbf{c}$, and $\mathbf{d}$ being real scalars and vectors, can be expressed in real form (for example, by combining with its complex conjugate, $\bar{\mathbf{z}}(t)$) as

$$\mathbf{x}(t) = e^{\gamma t}[\cos(\omega t)\mathbf{c} - \sin(\omega t)\mathbf{d}] \tag{1}$$

Thus a complex mode induces an oscillation with a continual transition from the shape $\mathbf{c}$ to the shape $\mathbf{d}$. The relative sizes and

[1]Corresponding author.

Contributed by the Design Engineering Division of ASME for publication in the Journal of Computational and Nonlinear Dynamics. Manuscript received October 12, 2011; final manuscript received September 15, 2012; published online May 14, 2013. Assoc. Editor: D. Dane Quinn.

degree of independence of **c** and **d** dictate the "amounts" of standing wave and traveling wave components.

Conversely, e.g., in a continuum, a sinusoidal wave motion, $y(x,t) = \sin k(x-ct) = \sin kx \cos \omega t - \cos kx \sin \omega t$, where $\omega = ck$, where k is the wave number, can be written as

$$y(x,t) = \mathrm{Re}[e^{i\omega t} \sin kx + ie^{i\omega t} \cos kx] = \mathrm{Re}(z(x,t)) \tag{2}$$

where the complex wave motion $z(x,t) = e^{i\omega t}[\sin kx + i \cos kx]$ perfectly matches the form of a continuous complex modal motion. When spatially discretized, the complex wave motion would be $\mathbf{z} = e^{i\omega t}[\mathbf{c} + i\mathbf{d}]$, where **c** is the spatially sampled $\sin kx$ and **d** is the spatially sampled $\cos kx$. Then $\mathbf{x} = (\mathbf{z} + \bar{\mathbf{z}})/2$ produces a real signal with the above interpretation.

2.3 Complex Orthogonal Decomposition. To apply the decomposition method, real measured signals $y(t)$ are first converted into complex analytic signals $z(t)$ by taking at the Fourier transform $\mathcal{F}(2y(t)) = 2\tilde{Y}(\omega)$, and reassigning the values of $2\tilde{Y}(\omega)$, for $\omega < 0$, to zero, to produce $\tilde{Z}(\omega)$. The inverse Fourier transform produces $z(t) = \mathcal{F}^{-1}(\tilde{Z}(\omega))$ [36]. Equivalently, if $y = \mathrm{Re}(z)$, then the $\mathrm{Im}(z)$ is the Hilbert transform of y, $\mathcal{H}(y)$ (e.g., [36]), and so $z(t) = y(t) + i\mathcal{H}(y(t))$. In practice, either calculation would involve the fast Fourier transform (FFT).

With signals in the complex form, $z_j(t)$, $j = 1, \ldots, M$, where M is the number of sensors distributed on a structure, we generate vectors $\mathbf{z}_j = [z_j(t_1) \cdots z_j(t_N)]^T$, by sampling at times t_1 through t_N. We build an $M \times N$ complex ensemble matrix $\mathbf{Z} = [\mathbf{z}_1 \cdots \mathbf{z}_M]^T$.

We construct a complex correlation matrix $\mathbf{R} = (1/N)\mathbf{Z}\bar{\mathbf{Z}}^T$, where the bar indicates complex conjugation. Since **R** is complex and Hermitian ($\mathbf{R} = \bar{\mathbf{R}}^T$), it has real eigenvalues and complex eigenvectors, and its normalized eigenvectors $\mathbf{u}_i$ are *unitary* (complex orthogonal) and satisfy

$$\bar{\mathbf{u}}_i^T \mathbf{u}_j = 0 \qquad i \neq j \tag{3}$$

The eigenvectors $\mathbf{u}_j$ of **R** are the complex orthogonal modes (COMs) and the eigenvalues λ_j are the complex orthogonal values (COVs). Thus, complex orthogonal decomposition refers to the construction of **R** and its eigenvalue problem.

For interpretation, suppose we have a complex signal, $z(x,t)$ measured in meters, to be spatially discretized at $x_1, \ldots, x_M$, where $x_i = i\Delta x$, $\Delta x = L/M$, and L is the length of the medium. Then $z(x,t) = \sum_{j=1}^{k} q_j(t)\phi_j(x)$, where ϕ_j are the normal modal functions to be discretized and approximately extracted, and $q_j(t) = f_j e^{i\omega_j t}$ are the k contributing harmonic modal coordinates. In the uniform case with orthogonal modal functions, $\int_0^L \phi_j(x)\bar{\phi}_j(x)dx = 1 \approx \underline{\hat{\phi}}_j^T \underline{\hat{\phi}}_j \Delta x$, where approximate modal vectors $\underline{\hat{\phi}}_j$ are generated from spatial sampling of the orthogonal complex modal functions, $\phi_j(x)$. Let us *renormalize* the modal vectors as $\underline{\phi}_j = \underline{\hat{\phi}}_j \sqrt{\Delta x}$, such that $\underline{\phi}_j^T \underline{\phi}_j = 1$ (implying that the $\underline{\phi}_j$ are dimensionless). Then the spatially discretized complex displacement vector can be written as $\mathbf{z} = \Phi \mathbf{q}_m$, where Φ is an $M \times M$ modal matrix, and $\mathbf{q}_m$ is the modal coordinate vector (implying that the units of $\mathbf{q}_m$ are m). The signal is uniformly sampled at times $t = t_1, \ldots, t_N$. As such, the ensemble has the form $\mathbf{Z}_{M\times N} = \Phi \mathbf{Q}_m$, where $\mathbf{Q}_m$ is an $M \times N$ ensemble matrix of sampled modal coordinates.

Applying this formulation to the analysis in [1], for orthogonal harmonic waves, if $\omega_j \neq \omega_k$, and if $\omega_j - \omega_k \neq 2\pi n/\Delta t$ for some integer n, then the discretized modal function is an approximate eigenvector of the complex correlation matrix **R**, such that $\mathbf{u}_j \approx \underline{\phi}_j$, and the associated eigenvalue is $\Lambda_j \approx d_j$, where $d_j = (1/N)\sum_{l=1}^{N} q_j(t_l)\bar{q}_j(t_l)$ is the mean squared magnitude of $q_j(t)$. If **z** is in meters, then the units of Λ_j are m^2. From Eq. (3), the mean squared magnitude $\langle |\underline{\phi}_j|_k^2 \rangle$ of an element k of the normalized eigenvector is $1/M$. Thus, for the kth particle on the medium, the expected mean squared displacement amplitude associated with the jth mode is $\langle |z_j(t)| \rangle = |q_j(t)|^2 \langle |\underline{\phi}_j|_k^2 \rangle = d_j/M \approx \Lambda_j/M$. The quality of these approximations depends on the sample resolution, i.e., M and N.

Thus, in the example of orthogonal waveforms with harmonic modulations, the complex orthogonal decomposition extracts the complex harmonic waveforms as the COMs and the mean squared modulations as the COVs through the eigenvalue problem associated with the complex correlation matrix **R**. These modulations of the complex modes define modal coordinates.

Similar to $\mathbf{Z} = \Phi \mathbf{Q}_m$, we can define $\mathbf{Z} = \mathbf{U}\mathbf{Q}$, where **U** is the matrix of COMs, and **Q** is the ensemble of complex orthogonal modal coordinates. If the modes in **U** are normalized, then by complex orthogonality (3),

$$\mathbf{Q} = \bar{\mathbf{U}}^T \mathbf{Z}$$

This is a *complex modal coordinate ensemble matrix*, the rows of which are the samples of each modal coordinate, $q_j(t)$, sampled at $t = t_1, \ldots, t_N$. The normalized vectors making up **U** are unitless, and so the units of **Q** are the same as those of **Z**.

COD is a generalization of POD, and will be able to extract both *standing and traveling* waves, as interpreted from the extracted complex modes. For POD to recover information about traveling and standing waves requires additional processing of the proper orthogonal modal coordinates, and recognizing whether two coordinates have the same frequencies and are 90 deg out-of-phase. However, the COD will pair these components together, automatically, as real and imaginary parts of a single complex vector. POD can yield equivalent traveling wave components only when the real and imaginary wave components are orthogonal, and only a limited number of wave modes can be captured.

2.4 Effects of Noise. Noise can be an issue in both biological and structural systems. Suppose the complex signal has low-level noise in addition to pure modal content, such that $\mathbf{Z} = \Phi \mathbf{Q}_m + \epsilon \mathbf{E}$, where ϵ is "small," and $\epsilon\mathbf{E}$ is the ensemble of added noise, which can in turn be written via a modal expansion as $\mathbf{E} = \Phi \mathbf{Q}_e$, with normalized orthogonal matrix Φ. Then the complex correlation matrix can be written as

$$\begin{aligned} N\mathbf{R} = \mathbf{Z}\bar{\mathbf{Z}}^T &= (\Phi\mathbf{Q}_m + \epsilon\mathbf{E})(\bar{\mathbf{Q}}_m^T\bar{\Phi}^T + \epsilon\bar{\mathbf{E}}^T) \\ &= \Phi\mathbf{Q}_m\bar{\mathbf{Q}}_m^T\bar{\Phi}^T + \epsilon\Phi\mathbf{Q}_m\bar{\mathbf{E}}^T + \epsilon\mathbf{E}\bar{\mathbf{Q}}_m^T\bar{\Phi}^T + \epsilon^2\mathbf{E}\bar{\mathbf{E}}^T \end{aligned}$$

the latter term of which is very small and negligible. As such, $N\mathbf{R} = \Phi\mathbf{Q}_m\bar{\mathbf{Q}}_m^T\bar{\Phi}^T + O(\epsilon)$, and for a set of eigenvalues that are well separated and not of order ϵ, the associated eigenvectors of **R** are perturbed by $O(\epsilon)$ [37], such that the noise-polluted eigenvectors are $\mathbf{v}_i = \underline{\phi}_i + \epsilon\mathbf{e}_i$.

Writing the COM as $\mathbf{v}_i = \underline{\phi}_i + \epsilon\mathbf{e}_i$, then $\mathbf{z}(t) = \mathbf{V}\mathbf{p}(t) = [\underline{\phi}_1 + \epsilon\mathbf{e}_1, \underline{\phi}_2 + \epsilon\mathbf{e}_2, \ldots, \underline{\phi}_M + \epsilon\mathbf{e}_M]\mathbf{p}$, where $\mathbf{p}(t)$ and **V** are the noise polluted complex-orthogonal modal coordinate vector and modal matrix as obtained by COD. By orthogonality of the COMs, $\mathbf{p}(t) = \bar{\mathbf{V}}^T\mathbf{z}(t)$, whence

$$p_i(t) = \underline{\hat{\phi}}_i^T\mathbf{z}(t) + \epsilon\bar{\mathbf{e}}_i^T\mathbf{z}(t) = q_i(t) + \epsilon\bar{\mathbf{e}}_i^T\mathbf{z}(t) \tag{4}$$

using $\underline{\hat{\phi}}_i^T\underline{\phi}_j = \delta_{ij}$ (*discrete normalized* case). The modal error vector $\mathbf{e}_i$ can be written in terms of linear normal modes by using the expansion theorem [34], $\mathbf{e}_i = \sum_{j=1,j\neq i}^{M} r_j\underline{\phi}_j$. Hence,

$$p_i(t) = q_i(t) + \epsilon \sum_{j=1,j\neq i}^{M} r_j q_j(t) \tag{5}$$

Thus the noise-contaminated complex orthogonal modal coordinate $p_i(t)$ is polluted by other normal modal coordinates depending on the deviation of the COM $\mathbf{v}_i$ from the true $\underline{\phi}_i$, as well as the relative strengths of linear normal modal components $q_j(t)$. However, small-noise contaminated $p_i(t)$ and $\mathbf{v}_i$ should be

representative of the "pure" $q_i(t)$ and $\underline{\phi}_i$. If the "true" underlying modes $\underline{\phi}_i$ are not orthogonal, then an additional contribution of $q_j(t)$ to $\overline{p_i}(t)$ appears in Eq. (5).

2.5 Traveling and Standing Waves. A measure of nonsynchronicity, or "traveling index" for mixed traveling waves, was defined [1] as the reciprocal of the condition number between the real and imaginary parts, **c** and **d**, of the complex mode. If **c** and **d** are nearly parallel, or if either **c** or **d** is dominant, then the motion expressed by Eq. (1) will be nearly synchronous, and the reciprocal of the condition number between **c** and **d** will be small. Purely nonsynchronous (including traveling) harmonic waves will have orthogonal real and imaginary parts of the same magnitude, leading to a condition number of 1, and hence a traveling index of one. (A "traveling index" of 1 indicates nonsynchronicity, which may not always represent traveling wave behavior.) As the traveling index approaches zero, there is essentially one independent vector, representing purely standing motion. Mixed wave modes can also be dissected into standing (synchronous) and traveling (nonsynchronous) parts [1].

3 Nematode Studies

Next we study the characteristics of nematode movements using COD. Presented here are results for an individual wild-type nematode (i.e., of the standard genetic background), with an average length of $L = 0.824$ mm, corresponding to "wild type worm 16" of the database linked off of Ref. [19].

3.1 Data Preparation. The worm crawled on a nematode growth medium (NGM), which is an agar based gel. The NGM can affect worm behavior [10]; the recipes used here are given in [38]. The NGM had a thin lawn of *Escherichia coli* strain OP-50 that had been allowed to grow over night at 37 °C in a lysogeny broth [38] prior to being spread on the NGM. One hour after the lawn was spread on the NGM, the nematodes were recorded for up to 2 h. During this time, the lawn was thin enough that the nematodes crawled on the NGM without much mechanical influence from the lawn. The tracking was done in the morning at 20 °C under fluorescent lighting. The night before, the nematodes were selected from a clearly distinguished larval-four stage, such that by morning, all nematodes in the sample were young adults within a 12 h difference in age. The conditions described here can be repeated. However, variations across individual worms prompts the need for statistics across a population, which is done with metrics computed in a Matlab Analyzer program [18], but not yet with the COD.

The worm was monitored using the Caltech Wormtracker system [18,19], in which the *C. elegans* were videotaped in an optical tracking microscope. The videos were processed such that $(\hat{x}(t), \hat{y}(t))$ (planar) positions of $M = 13$ equally spaced virtual markers on the worms are identified, sampled and recorded. About 4 min of worm motion data were typically sampled at $\Delta t = 0.1666$ s per sample ($N = 1407$ total time samples). This process can be done for wild and mutant nematodes. Post processing of these data using the Analyzer program produces motion parameters such as velocities, bending frequencies, wavelengths, and track amplitudes (based on the size of the bounding box on a crawling worm) [18]. These quantitative characteristics can then be attached to the descriptions of various mutant behaviors [19], and compared to similar quantities obtained via the COD.

Let $\hat{\mathbf{x}}(t)$ and $\hat{\mathbf{y}}(t)$ be arrays of the $(\hat{x}(t), \hat{y}(t))$ coordinates of the 13 virtual markers on the wiggling worm. In preparation for the COD, first the center of mass of each sample of $\hat{\mathbf{x}}(t_i)$ and $\hat{\mathbf{y}}(t_i)$ data, for $i = 1, \ldots, 1407$, was translated to the origin. For each sample configuration, the principal axes were found by applying POD [29] to the 13 marker positions in the $\hat{x}$ and $\hat{y}$ space. Then the worm was rotated so that its principal axis lined up with the horizontal axis, while keeping a record of each rotation angle $\theta(t_i)$. This produced,

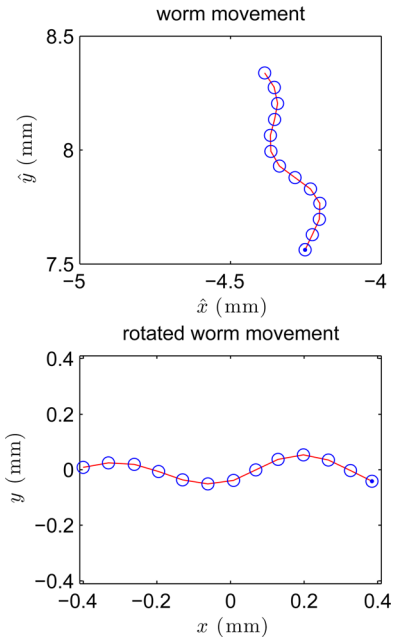

Fig. 1 Above is the captured worm, arbitrarily located and oriented. The head points down, and is indicated by a small dot. The coordinates are translated to the origin and rotated, as shown below, where *y* indicates the transverse deflection of the worm markers. The head (dot) points right.

for each time sample of each measured marker, a new (x, y) coordinate, such that x specifies the axial position and y indicates the transverse position of a marker (see Fig. 1). In the on-line paper, movie (Supplemental Movie 1) shows the animation of a short time segment of a crawling worm based on the locations of the virtual markers. Movie (Supplemental Movie 2) shows a short time segment of transverse displacements of each virtual marker. Time is sped up in movies (Supplemental Movies 1 and 2).

3.2 Modal Decomposition of Posturing Movements. This COD analysis was based on only the y (transverse) data, to ease visualization. This neglects axial contraction and extension which can also take place to some extent. As such, column i of the ensemble **Y** was built from the y values of the 13 markers at time t_i, with marker one corresponding to the head. The complex analytic ensemble **Z** was then created, and the COD was performed. The COVs indicated that two or three complex modes were significantly above the noise level (Fig. 2). These mode shapes and their modal coordinate dynamics were examined and are discussed below.

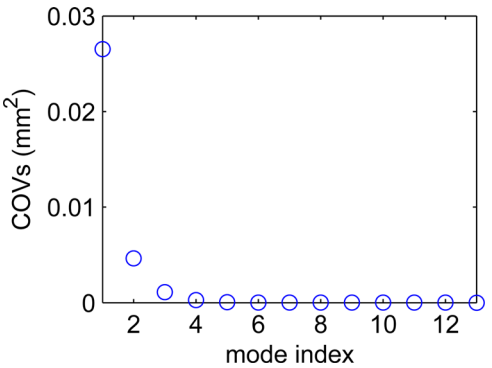

Fig. 2 The COVs showing relative mean squared modal amplitudes

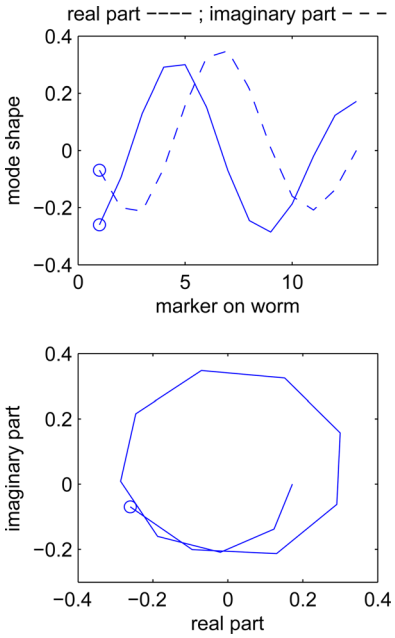

Fig. 3 Top: (dominant) mode one, with real (solid line) and imaginary (dashed line) parts. (The vertical axes are magnified compared to Fig. 1.) The head is at marker 1 (the circle) and points left. Bottom: mode one in the complex plane, where the head is marked with the circle.

3.2.1 Dominant Mode: Locomotion. The first mode, shown in Fig. 3, represents motion that, with an oscillatory modulation, alternates between the solid and dashed lines of the top figure, and their negatives, describing a traveling wave to the right. The marker at the head is represented by the small circle. The "traveling index" of this mode is 0.9387.

The dominant COV suggests a dominant average modal amplitude of about 0.16 mm. Considering that the first modal transverse motion is $\mathbf{z}_1(t) = q_1(t)\underline{\phi}_1$, the first modal motion of the kth virtual marker has the form $z_{1k} = q_1(t)\phi_{1k}$, and has an amplitude $|z_{1k}| = |q_1(t)||\phi_{1k}| = 0.16|\phi_{1k}|$ in mm. Except for the last two tail markers, $|\phi_{1k}| \approx 0.3$ in Fig. 3, and so $|z_{1k}| \approx 0.05$ mm. Peak-to-peak transverse motion is therefore about 0.098 mm, which is about 12% of the straightened worm's length. The Analyzer program produced a mean track amplitude of about 14.5% from the aspect ratio of the instantaneous bounding box of the captured worm. The methods produce slightly different measures of oscillation amplitude, and the results can be considered consistent.

From the complex plot of mode one (Fig. 3, bottom), we can estimate the wavelength as the portion of the worm's length that completes one full circle in the plot. Here the wavelength is about $\lambda = 0.69$ worm lengths per cycle. The wavelength can also be expressed in mm/cycle if λ is multiplied by the mean length of the worm, such that $\hat{\lambda} = L\lambda = 0.569$ mm/cycle. This represents the wavelength measured along the deformed axis of the worm. To obtain the wavelength measured in the crawling medium, we consider the amount of foreshortening under transverse deformation.

To quantify the foreshortening, suppose $y(x)$, with $x = 0$ at the head, represents the transverse displacement of a location x along an worm at a fixed moment in time. We approximate the worm as inextensible, under the assumption that the transverse deformations are significantly larger than axial deformations. When $y(x) = 0$ everywhere, the worm is straight, and defines an undeformed worm axis χ, which we visualize as horizontal. When $y(x)$ is arbitrarily deformed, the worm is foreshortened in the χ direction, and the projection, from the head to a point x on the worm, onto the χ axis has length $p(x)$. For a deflected differential element dx of the worm, dy is the rise in the element, dx is the hypotenuse, and dp is the run, such that $dp = \sqrt{(dx^2 - dy^2)} = \sqrt{(1 - (dy/dx)^2)}dx$. Using a Taylor series for small slopes, $dp/dx \approx 1 - (dy/dx)^2/2$. Approximating the worm posture as a sinusoid, such that $y(x) = A\sin(2\pi x/\hat{\lambda} + \phi)$, where $\hat{\lambda}$ is in mm/cycle, we can integrate to obtain the projected length of a single wavelength as $p(\lambda) = \lambda(1 - 2(\pi A/\lambda)^2)$. Using our estimated value of $A = 0.05$ mm we obtain $p(\hat{\lambda}) = 0.85\hat{\lambda}$. Then $p(\hat{\lambda}) = \hat{\lambda}_p = P\hat{\lambda}$, where $P = 0.85$, is the wavelength as measured *in the medium,* while the original wavelength $\hat{\lambda}$ was measured with respect to the deformed spinal axis of the worm.

It is informative to examine the modal coordinates, as well. The primary modal coordinate is persistently active; the mode represents locomotion. This modal coordinate has a consistent whirl in the complex plane. The real part of the modal coordinate is oscillatory, with a frequency equal to the whirl rate of the complex coordinate. The frequency can be estimated from the mean complex whirl rate of the modal coordinate ($f_w = 0.31$ Hz, with a standard deviation of 0.11) or the FFT ($f_{\mathrm{FFT}} = 0.32$ Hz) of the real part of the complex coordinate. The mean frequency estimated by the Analyzer program (short time FFT of nematode bending) is 0.31 Hz. The instantaneous whirl rate is computed and shown in Fig. 4, indicating that the worm has considerable variation, with apparent cruising speeds, as well as short bursts and lulls. The spectrum is also shown in Fig. 4, with the variation in oscillation rate contributing to the broadened frequency peak.

The wave speed is estimated as $v_w = \lambda f_w = 0.21$ worm lengths per second, or 0.173 mm/s on average. The mean centroid velocity from the Analyzer program is about 0.139 mm/s, about 80% of the estimated wave speed. The value v_w, a "mathematical wave speed" that results from the calculation in the complex plane through λ, can be interpreted as the speed of the wave through the deformed spinal axis of the worm. Applying the estimated foreshortening to calculate the wave speed of the projected wave form yields $v_p = \hat{\lambda}_p f_w = Pv_w = 0.147$ mm/s, such that the mean centroid velocity is now 95% of the projected wave speed. We can regard v_p as the wave speed as measured by an observer fixed to the medium. The 5% discrepancy could be caused by roundoff error in the estimate of A, small amounts of slip in the track, and also by the fact that the centroid speeds were averaged over the whole time record, which involves instances of nonlocomotive

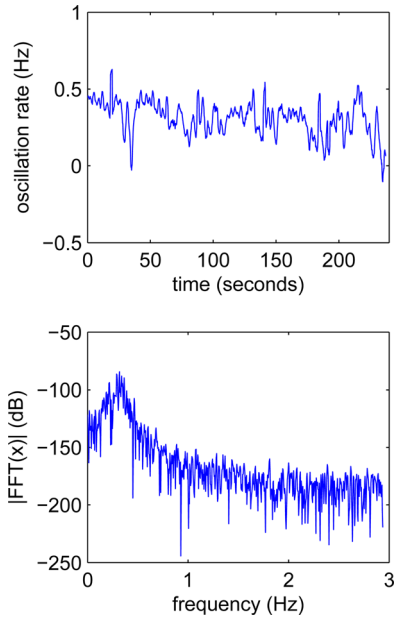

Fig. 4 Top: dominant mode oscillation frequency, taken from the complex whirl rate, over time. Bottom: spectrum of the dominant modal coordinate, where dB is computed as 20 log $q_1(t)$, and where q_1 is in mm.

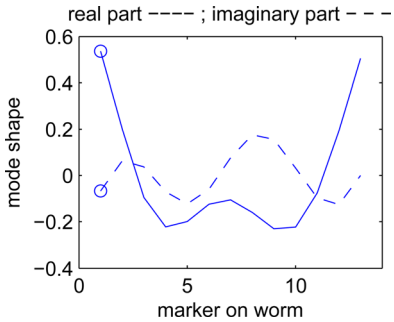

Fig. 5 Mode two, with real (solid line) and imaginary (dashed line) parts. (The vertical axes are magnified compared to Fig. 1.) The circle indicates the head marker.

modes. This is addressed later in Sec. 3.3. Generally, we expect the wave speed to nearly represent the worm's speed since not much slipping is observed in the worm's track.

3.2.2 Second Mode. The second mode is shown in Fig. 5. The traveling index is 0.3589, and thus it has more standing qualities than the first mode. The second mode is intermittently active. The occurrence of activity in this mode is strongly correlated with changes in $\theta(t)$, suggesting that this mode represents a steering effort. This can be seen by looking at the heading angle and its change (red and black solid curves of Fig. 6, top), along with the real part of the second modal coordinate $q_2(t)$ (magenta/lighter curve, overlapping the black curve). The time derivative of the heading angle is approximated by finite differences over a 60-sample range, or about a 10-s range, which covers on average about three primary-mode cycles, and is scaled by a factor of 10 in Fig. 6 for visualization. The real part of the second modal coordinate is plotted as its moving average over 60 samples (or 10 s). As the modal vectors are normalized to an amplitude of one, and are unitless, the modal coordinates are in mm. The plot of the moving-averaged second modal coordinate $q_2(t)$ is scaled by a factor of 10 to visually bring forth the correlation between $q_2(t)$ and the change in heading angle. The product $q_2(t)\dot{\theta}(t)$ between the moving-averaged second modal coordinate and the change in heading angle is shown in Fig. 6 (bottom). The positive bias in this graph, and the correlation coefficient $\rho_{q_2\dot{\theta}} = E[(q_2(t) - \bar{q}_2)(\dot{\theta}(t) - \bar{\dot{\theta}})]/(\sigma_{q_2}\sigma_{\dot{\theta}}) = 0.70$, suggest a strong correlation ($\rho = 0$ indicates no correlation, and $|\rho| = 1$ indicates perfect correlation [39]).

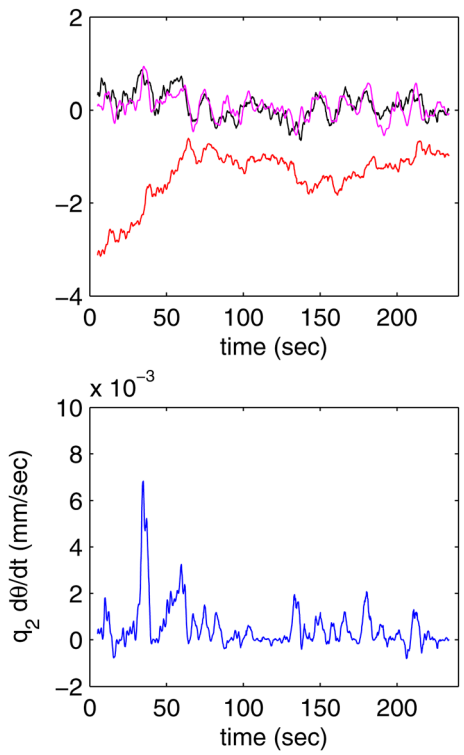

Fig. 6 Top: the heading angle $\theta(t)$ (lower isolated curve, in red) in radians; the scaled change in angle $10\dot{\theta}(t)$ (black, overlapping), in radians, computed by finite differences; and the real part of the scaled moving-averaged second modal coordinate $10q_2(t)$ (magenta/light, overlapping) in mm. Bottom: the product of the second modal coordinate and the change in heading angle. $q_2(t)\dot{\theta}(t)$, in mm per second.

Indeed, the second-mode motion can be re-animated by modulating the second complex mode with the second complex modal coordinate, such that the activity of the second mode is isolated, and by adding the heading angle $\theta(t)$ back into the motion, the correlation of second-mode activity and angular changes can be witnessed. A short segment of such motion, sped up, is shown in movie (Supplemental Movie 3) of the on-line version.

3.2.3 Third Mode. The third mode is shown in Fig. 7(*a*). The mode shape can be interpreted as similar to the first, although noise polluted, but the real and imaginary parts are oppositely phased, implying that it may be for reverse motion. A wavelength of $\lambda = 0.621$ worm lengths per cycle was estimated from the complex whirl. The traveling index of 0.9248 suggests a strongly traveling mode. To consider the possibility of its role as a reverse locomotion mode, the "heading speed" (dotted curve) and the third modal coordinate activity (solid line) are shown in Fig. 7(*b*). The "heading speed" is computed as the inner product between centroid velocity and the unit vector in the direction of the heading angle. As such, the heading speed is positive when in forward locomotion, and negative when in reverse. This worm does not do much reverse during the 4-min time record. However, the reverse activity during the last minute is coincident with bursts of third mode activity. These bursts can be seen clearly although the entire third modal coordinate is rather heavily noise polluted, which is not surprising in regard to Sec. 2.4 since it is a low-energy mode

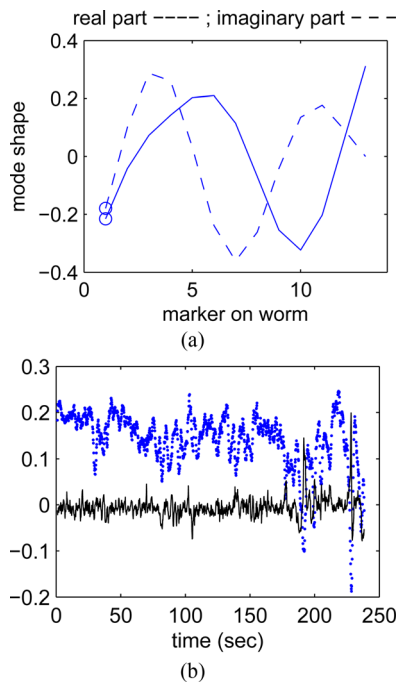

Fig. 7 (*a*) Mode three, with real (solid line) and imaginary (dashed line) parts. The circle indicates the head marker. (*b*) The upper dotted curve shows the instantaneous centroid heading speed in mm/s, and the lower solid curve shows the third modal coordinate history.

(about 3% of the signal energy, defined here as the sum of the COVs, which we recall to be the modal amplitudes squared). The modal pollution over the entire history, combined with the few reversal events, reduces the significance of a correlation coefficient calculation. However, the features in Figs. 7(*a*) and 7(*b*) support the interpretation of the third mode.

3.3 Short-Time Analysis of Locomotion. The above decompositions were applied to the entire time record. Hence, the wave mode shapes represent spatial distributions associated with forward locomotion, steering, and reverse locomotion, averaged in some way over the whole time record. The decomposition can be staged to generate information on the temporal variation of these spatial distributions by applying the decomposition to subintervals of the complex analytic time record.

Here we define the time interval for the short-time decomposition as $T = k\tau$, where $\tau = 1/f_w = 3.2$ s is the period associated with the mean oscillation frequency of the dominant (locomotion) modal coordinate over the whole time record. The number of sampling indices for the interval is then $N_T = \lceil T/\Delta t \rceil$, where the brackets indicate the integer ceiling function. This time window is centered at the sampling index i_c, and the analysis is performed at values of i_c starting at $i_0 = \lceil i_T/2 \rceil$ and ending at $i_f = N - i_0$, with i_c increasing at unit increments. As such, there are a total of $N_k = N - N_T$ overlapping windows. We analyze the dominant mode of each window. The overlapping leads us to expect typically continuous variations in estimated features, such as wavelength.

T is a parameter in the analysis procedure. If T is small, it refines the temporal resolution of the variation in motion features. However, if T is smaller than a period of oscillation, or if T is small but not commensurate with the ongoing oscillation period, there could be some distortion in the features. We worked with subintervals of the complex analytic ensemble, rather than obtaining a complex analytic ensemble from subintervals of the real ensemble, to avoid endpoint effects of leakage that would result from the Hilbert transform, or the FFT and its inverse, of a small subinterval. If T is large, temporal resolution would be coarse, features would be averaged over larger time records, and variations of features of motion would thus be filtered.

Thus, we would like to make T as small as possible without introducing significant distortions. We ran short time decompositions for $T = k\tau$, with assorted values of k from 1 through 16. For example, with $T = \tau$ (i.e., $k = 1$), we obtained an average wavelength of $\lambda_1 = 0.692$ worm lengths per cycle with a standard deviation of $\sigma_{\lambda 1} = 0.114$, and an average oscillation frequency $f_1 = 0.297$ cycle/s with $\sigma_{f1} = 0.101$. (The "average" value f_1 was obtained as the average of $N_1 = 1387$ values of mean complex whirl rates of the modal coordinates of the short-time decompositions. The value of σ_{f1} was the standard deviation of these mean short-time whirl rates.) The average of the mean short-time centroid velocities was $v_1 = 0.139$ mm/s with $\sigma_{v1} = 0.046$, compared to the product $v_{1w} = \hat{\lambda}_1 f_1 = 0.1644$ mm/s, which represents the wave speed through the spinal axis, and $v_{1p} = P v_{1w} = 0.140$ mm/s as the wave speed seen by an observer in the NGM.

For $T = 3\tau$, from $N_3 = 1349$ overlapping short-time windows, we obtained $\lambda_3 = 0.704$ worm lengths per cycle with a standard deviation of $\sigma_{\lambda 3} = 0.146$, and an average $f_3 = 0.307$ cycle/s with $\sigma_{f3} = 0.079$. In this case the average of the mean short-time centroid velocity was $v_3 = 0.139$ mm/s with $\sigma_{v3} = 0.043$, which is about 80% of the spinal wave speed $v_{3w} = \lambda_3 f_3 = 0.174$ mm/s. The mean projected wave speed was $v_{3p} = 0.148$ mm/s, and the standard deviation was $\sigma_{3p} = 0.034$. The variation of wavelength, and the short-time averaged centroid velocity, projected wave speed (v_{3p}), and frequency for $T = 3\tau$ are shown in Fig. 8. The plot shows that there is mostly continuous variation in the wavelength, except for some isolated spikes which reach values off the scale of the graph to about 1.8 worm lengths per cycle. The spikes occur in the vicinity of a lull in speed and frequency, also near a time in which the worm had a short instance of reverse locomotion (Fig. 7). It is likely that the spikes in wavelength correspond to instances when the locomotion mode is not dominant, giving way to another mode (such as reverse). In such an instance, perhaps the transition distorts the short-time extracted modes. The histogram of wavelengths is also shown in Fig. 8. Most of the wavelength activity is near the mean wavelength, while a few occurrences at higher wavelengths are present. These features are qualitatively consistent with those in [19]. These higher wavelengths likely represent brief instants of nonlocomotive activity.

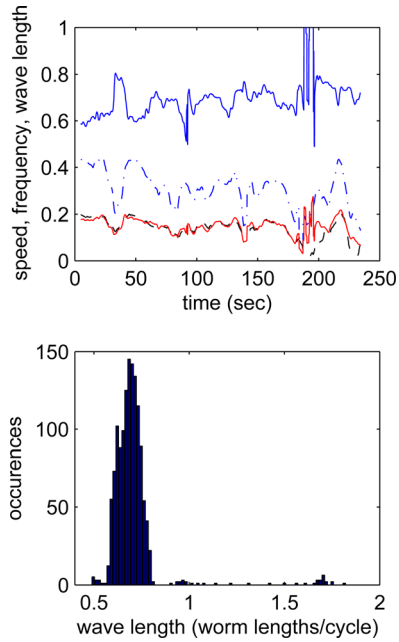

Fig. 8 The upper plot shows the temporal variation of the first-mode wavelength in worm lengths per cycle (top solid curve), centroid speed in mm/s (dashed curve), projected wave speed in mm/s (lower solid curve), and dominant modal coordinate frequency in Hz (dashed-dotted curve) from short-time decompositions with $T = 3\tau$. The lower plot shows a histogram of the short-time averaged wavelengths.

For these data, calculations with $T = \tau$ through $T = 4\tau$ produced these spikes in the short-time average wavelength plots. For $T \geq 4.5\tau$ and higher, these spikes of higher wavelength were not produced. It is likely that if the short-time interval is long enough, then mode changes, such as reversals, do not dominate the interval, and the locomotion mode remains primary.

For $T = 5\tau$, from $N_5 = 1311$ short-time windows, we obtained $\lambda_5 = 0.686$ worm lengths per cycle with a standard deviation of $\sigma_{\lambda 5} = 0.043$, and an average $f_5 = 0.308$ cycle/s with $\sigma_{f5} = 0.061$. In this case the average of the mean short-time centroid velocity was $v_5 = 0.139$ mm/s with $\sigma_{v5} = 0.035$, again 80% of the spinal wave speed $v_{5w} = \hat{\lambda}_5 f_5 = 0.173$ mm/s, while the mean projected wave speed was $v_{5p} = 0.147$ mm/s with $\sigma_{5p} = 0.025$.

Figure 9 shows the short-time features for $T = 5\tau$. In this case, the spikes in estimated short-time wavelength values are not present near the lull in locomotor activity. The wavelength has a continuous temporal variation. The histogram is centered at the mean wavelength.

With a focus on the locomotion mode, the plots for $T = 3\tau$ have some distortions, higher temporal resolution, but more variation, compared to the plots for $T = 5\tau$. There are some trends that are common among plots for a wide range T, including T not shown. In all cases, the estimations for wavelength, frequency and wave speed were consistent with the estimations $\lambda = 0.69$ worm lengths per cycle, $f_w = 0.31$ Hz, the spinal wave speed $v_w = \hat{\lambda} f_w = 0.173$ mm/s, and the projected wave speed of $v_p = 0.147$ mm/s, obtained from the entire time record. Apparent

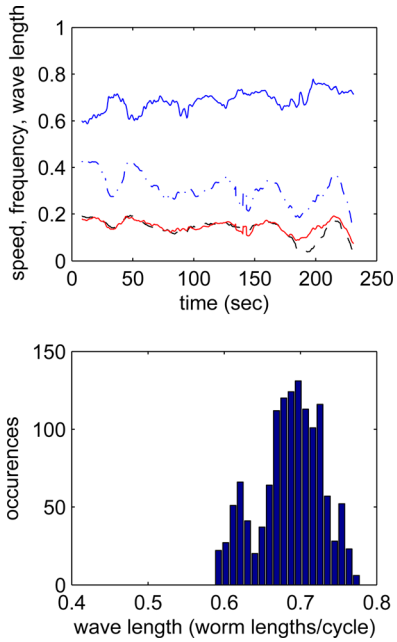

Fig. 9 The upper plot shows the temporal variation of the first-mode wavelength in worm lengths per cycle (top solid curve), centroid speed in mm/s (dashed curve), projected wave speed in mm/s (lower solid curve), and dominant modal coordinate frequency in Hz (dashed-dotted curve) from short-time decompositions with $T = 5\tau$. The lower plot shows a histogram of the short-time averaged wavelengths.

in the temporal variation plots, for example, Fig. 9, is a trend for gradually increasing wavelength, and gradually decreasing speed and frequency, over time. These trends occur amid a short-time fluctuation in these features. It may be possible that either these gradual trends are related due to mechanics or behavior of crawling, or the gradual trends are not directly related, but are influenced by an evolving state or environment of the worm. The product, which is the wave speed, follows the frequency profile more than the wavelength profile. After $t = 175$ s for $T = 5\tau$ and $t = 180$ s for $T = 3\tau$, near the lull in speed, these trends are disrupted. Also, the average projected wave speed, v_p, was very close to the average centroid velocity. For the plotted calculations associated with $T = 3\tau$ and $T = 5\tau$, the average centroid velocity closely followed the projected wave speed, again suggesting that crawling happened with little slip, when the posturing was mostly focused on locomotion prior to the disruption at $t = 175 - 180$ s.

Estimations of mean wavelength, frequency, and wave speed, are also robust over a wide range of T, and are close to the values estimated from a decomposition over the entire time record. The histograms show some variation in the fine distribution of occurrences among bins (about 20 span the locomotion wavelength) as T varies. As T increases, the temporal variation about the temporal trend is filtered. Accordingly, the standard deviation of the wavelength, frequency, and speed reduces as T increases. The standard deviation in wavelength undergoes a marked reduction as the high-wavelength spikes disappear with increasing T.

4 Conclusion

A crawling nematode produces a complicated traveling wave in its posturing patterns. Complex mode representations of the motion patterns allow the worm's waveforms to be described with fixed real and imaginary parts, which is an alternative to animated descriptions of the wave patterns. The COD tool for decomposing mixed traveling and standing complex wave modes extracts modes as optimal distributions of signal energy, and was thus applied to the posturing patterns of a wild *C. elegans* nematode.

The COD indicates that the worm had a multimodal posturing behavior, involving at least a forward locomotion mode, a steering mode, and probably a backward locomotion mode. Here, "mode" means a characteristic shape and action associated with these maneuvers. The locomotion mode was dominant in terms of its mean squared modal amplitude, and it was shown to be closer to a pure traveling waveform than the steering, secondary mode. Although the reverse locomotion mode was seldom active in this data record, evidence of its existence includes the similarity to the forward mode but with a phase reversal, and the coincidence of strong third modal coordinate activity with the brief instances of backward crawling of this worm. This reverse mode consisted of about 3% of the signal energy, and its modal coordinate was rather noise polluted. A discussion of the effects of small levels of noise on the COD was included.

Motion parameters, such as wavelength, frequency, wave speed, and amplitude, of the isolated primary locomotion mode were estimated. These parameters compared favorably with those metrics computed previously with the Analyzer program. The analysis approaches are complementary, and the overlapping quantities provide a means for cross checking between each analysis package. In the modal analysis approach, wavelength was estimated from the extracted complex mode shapes, and the frequency was obtained from the complex modal coordinate's complex whirl rate, and from its FFT. The estimated wavelength represented an average modal behavior over the data record used in the decomposition. The average wave speed was first computed as the speed along the deformed spinal axis of the worm. Accommodating foreshortening led to an estimation of the wave speed in the medium, which compared very well with the centroid speed, suggesting minimal slip while crawling forward on the NGM.

Temporal variation of wavelength and frequency were obtained by applying the decomposition over many shorter time record windows. The short-time feature estimations were affected by the length T of the short-time interval, but the trends in the features were consistent, and the overall averages matched the estimations from decompositions of the entire time record. These calculations showed that the wavelength exhibited a trend to increase over time, while the modal coordinate oscillation frequency decreased slowly over time, and that short-time fluctuations of wavelength were opposite those of frequency.

This paper has demonstrated the application of an analysis method to a single data set of a single worm. In future work, the COD can be used in concert with metrics from the Analyzer program to describe spatio-temporal characteristics of behavior patterns over a population of worms. It may also be used to describe characteristics of normal and abnormal posturing motions, which can then be connected to the study of genetic mutations on phenotypes associated with the posture patterns of wild-type *C. elegans*.

Acknowledgment

This work was supported in part by the National Institutes of Health (Grant No. USPHS DA018341) and was related in part to a project with the National Science Foundation (CMMI-0727838). Any opinions, findings, and conclusions or recommendations are those of the authors and do not necessarily reflect the views of the NSF.

References

[1] Feeny, B. F., 2008, "A Complex Orthogonal Decomposition for Wave Motion Analysis", J. Sound Vib., **310**(1–2), pp. 77–90.

[2] NIH-National Human Genome Research Institute, "International Genome Team Deciphers Genetic Instructions for a Complete Animal," ScienceDaily, 11 December 1998, Retrieved Feb. 6, 2008, http://www.sciencedaily.com/releases/1998/12/981211084627.htm

[3] Mendel, J. E., Korswagen, H. C., Liu, K. S., Hajdu-Cronin, Y. M., Simon, M. I., Plasterk, R. H. A., and Sternberg, P. W., 1995, "Participation of the Protein Go in Multiple Aspects of Behavior in *C. elegans*," Science, **267**, pp. 1652–1655.

[4] Jorgensen, E. M., 2005, "GABA," WormBook, August 31:1–13, http://www.wormbook.org
[5] Bastiani, C., and Mendel, J., 2006, "Heterotrimeric G Proteins in *C. elegans*," WormBook, 2006 Oct 13:1–25, http://www.wormbook.org
[6] Rand, J. B., 2007, "Acetylcholine," WormBook, 2007 Jan 30:1–21, http://www.wormbook.org
[7] Chase, D. L., and Koelle, M. R., 2007, "Biogenic Amine Neurotransmitters in *C. elegans*," WormBook, 2007 Feb 20:1–15, http://www.wormbook.org
[8] Li, W., Feng, Z., Sternberg, P. W., and Xu, X. Z. S., 2006, "A *C. elegans* Stretch-Sensitive Neuron Revealed by a Mechanosensitive TRP Channel Homologue," Nature, **440**, pp. 684–687.
[9] Van Buskirk, C., and Sternberg, P. W., 2007, "EGF Signaling Induces Behavioral Quiescence in *C. elegans*," Nature Neurosci., **10**, pp. 1300–1307.
[10] Karbowski, J., Cronin, C. J., Seah, A., Mendel, J. E., Cleary, D., and Sternberg, P. W., 2006, "Conservation Rules, Their Breakdown, and Optimality in *Caenorhabditis* Sinusoidal Locomotion," J. Theor. Biol., **242**, pp. 652–669.
[11] Karbowski, J., Schindelman, G., Cronin, C. J., Seah, A., and Sternberg, P. W. 2008, "Systems Level Circuit Model of *C. elegans* Undulatory Locomotion: Mathematical Modeling and Molecular Genetics," J. Comput. Neurosci., **24**, pp. 253–276.
[12] Boyle, J. H., and Cohen, N., 2008, "*Caenorhabditis elegans* Body Wall Muscles Are Simple Actuators," BioSystems, **94**, pp. 170–181.
[13] Boyle, J. H., Bryden, J., and Cohen, N., 2008, "An Integrated Neuro-Mechanical Model of *C. elegans* Forward Locomotion," Lect. Notes Comput. Sci., **4984**, pp. 37–47.
[14] Haspel, G., O'Donovan, M. J., and Hart, A. C., 2010, "Motoneurons Dedicated to Either Forward or Backward Locomotion in the Nematode *Caenorhabditis elegans*," J. Neurosci., **30**(33), pp. 11151–11156.
[15] Korta, J., Clark, D. A., Gabel, C. V., Mahadevan, L., and Samuel, A. D. T., 2007, "Mechanosensation and Mechanical Load Modulate the Locomotory Gait of Swimming *C. elegans*," J. Exp. Biol., **210**, pp. 2383–2389.
[16] Pierce-Shimomura, J. T., Chen, B. L., Mun, J. J., Ho, R., Sarkis, R., and McIntire, S. L., 2008, "Genetic Analysis of Crawling and Swimming Locomotory Patterns in *C. elegans*," Proc. Natl. Acad. Sci., **105**(52), pp. 20982–20987.
[17] Berri, S., Boyle, J. H., Tassieri, M., Hope, I. A., and Cohen, N., 2009, "Forward Locomotion of the Nematode *C. elegans* is Achieved Through Modulation of a Single Gait," HFSP J., **3**(3), pp. 186–193.
[18] Feng, Z., Cronin, C. J., Wittig, Jr., J. H., Sternberg, P. W., and Schafer, W. R., 2004, "An Imaging System for Standardized Quantitative Analysis of *C. elegans* Behavior," BMC Bioinformatics, **5**, p. 115.
[19] Cronin, C. J., Mendel, J. E., Muhktar, S., Kim, Y.-M., Stirbl, R. C., Bruck, J., and Sternberg, P. W., 2005, "An Automated System For Measuring Parameters of Nematode Sinusoidal Movement," BMC-Genetics, **6**, p. 5.
[20] Lumley, J. L., 1970, *Stochastic Tools in Turbulence*, Academic Press, New York.
[21] Berkooz, G., Holmes, P., and Lumley, J. L., 1993, "The Proper Orthogonal Decomposition in the Analysis of Turbulent Flows," Annu. Rev. Fluid Mech., **25**, pp. 539–575.
[22] Cusumano, J. P., and Bai, B.-Y., 1993, "Period-Infinity Periodic Motions, Chaos, and Spatial Coherence in a 10 Degree of Freedom Impact Oscillator," Chaos, Solitons, and Fractals, **3**(5), pp. 515–535.
[23] Epureanu, B. I., Tang, L. S., and Paidoussis, M. P., 2004, "Exploiting Chaotic Dynamics for Detecting Parametric Variations in Aeroselastic Systems," AIAA J., **42**(4), pp. 728–735.
[24] FitzSimons, P., and Rui, C., 1993, "Determining Low Dimensional Models of Distributed Systems," *Advances in Robust and Nonlinear Control Systems*, ASME DSC-Vol. **53**, pp. 9–15.
[25] Kerschen, G., Golinval, J. C., Vakakis, A. F., and Bergman, L. A., 2005, "The Method of Proper Orthogonal Decomposition for Dynamical Characterization and Order Reduction of Mechanical Systems: An Overview," Nonlinear Dynamics, **41**(1–3), pp. 147–169.
[26] Yasuda, K., and Kamiya, K., 1997, "Experimental Identification Technique of Nonlinear Beams in Time Domain," ASME Design Engineering Technical Conferences, Sacramento, CA, CD-ROM.
[27] Ma, X., Azeez, M. A. F., and Vakakis, A. F., 2000, "Nonlinear Normal Modes and Nonparametric System Identification of Nonlinear Oscillators," Mech. Syst. Signal Proc., **14**(1), pp. 37–48.
[28] Liang, Y. C., Lee, H. P., Lim, S. P., Lin, W. Z., Lee, K. H., and Wu, C. G., 2002, "Proper Orthogonal Decomposition and its Applications—Part 1: Theory," J. Sound Vib., **252**(3), pp. 527–544.
[29] Feeny, B. F., and Kappagantu, R., 1998, "On the Physical Interpretation of Proper Orthogonal Modes in Vibrations," J. Sound Vib., **211**(4), pp. 607–616.
[30] Feeny, B. F., 2002, "On the Proper Orthogonal Modes and Normal Modes of Continuous Vibration Systems," ASME, J. Vib. Acoust., **124**(1), pp. 157–160.
[31] Kerschen, G., and Golinval, J. C., 2002, "Physical Interpretation of the Proper Orthogonal Modes Using the Singular Value Decomposition," J. Sound Vib., **249**(5), pp. 849–865.
[32] Feeny, B. F., and Liang, Y., 2003, "Interpreting Proper Orthogonal Modes in Randomly Excited Vibration Systems," J. Sound Vib., **265**(5), pp. 953–966.
[33] Feeny, B. F., 2012, "Complex Modal Decomposition for Estimating Wave Properties in One-Dimensional Media" J. Acoust. Vib., (to be published).
[34] Meirovitch, L., 1997, *Principles and Techniques in Vibrations*, Prentice-Hall, NJ.
[35] Ginsberg, J., 2001, *Mechanical and Structural Vibrations*, Wiley, New York.
[36] Oppenheim, A. V., and Schafer, R. W., 1989, *Discrete-Time Signal Processing*, Prentice-Hall, Englewood Cliffs, NJ.
[37] Noble, B., and Daniel, J. W., 1977, *Applied Linear Algebra*, Prentice-Hall, Englewood Cliffs, NJ.
[38] Stiernagle, T., 2006, "Maintenance of *C. elegans*," Wormbook, The C. elegans Research Community, doi/10.1895/wormbook. 1.101.1, http://www.wormbook.org
[39] Newland, D. E., 1993, *An Introduction to Random Vibrations, Spectral and Wavelet Analysis*, 3rd ed., Longman Scientific and Technical, Singapore.